Petrology of banded iron formation-related country rocks at the northern limit of the Mbalam iron ore district, southeastern Cameroon

Akumbom Vishiti*[1,2], Dieudonne Charles Isidore Ilouga [3], Ndzegha Collins Bomyoymoah[4], Cheo Emmanuel Suh[4,5]

[1]Department of Civil Engineering, The University Institute of Technology (IUT), University of Douala, P.O. Box 8698, Douala, Cameroon

[2]Laboratory of Geosciences, Natural Resources and Environment, Department of Earth Sciences, Faculty of Science, University of Douala, P.O. Box 24157, Douala, Littoral Region, Cameroon

[3]Geology Laboratory, Higher Teacher Training College (ENS), University of Yaoundé I, P.O. Box 047, Yaoundé, Cameroon

[4]Department of Geology, Mining and Environmental Science, The University of Bamenda, P.O. Box 39 Bambili, North West Region Cameroon

[5]Economic Geology Unit, Department of Geology, University of Buea, P.O. Box 63, Buea, Cameroon

*__Corresponding author email:__vakumbom@gmail.com

ABSTRACT

Banded iron formation (BIF)-related country rocks at the northern limit of the Mbalam iron ore district constitute part of the Archean to Proterozoic greenstone belt of the Congo Craton (CC). In this study the petrology of BIFs and amphibolites from the lower part of the Njweng ridge is presented in a bid to decipher the source of the sediments and their inherent iron enrichment. The BIFs vary from oxide to silicate facies categories, composed mainly of magnetite bands alternating with quartz bands and their mineralogy is dominated by magnetite, hematite and quartz. The amphibolites contain quartz, magnetite, amphibole, biotite, garnet with a distinct schistocity. The Fe_2O_3 and SiO_2 content of the BIFs reach highs of 54.55 wt% and 57.83 wt%, respectively. The average Fe_2O_3 content of 46.7 wt% coupled with SiO_2 and Al_2O_3 as deleterious elements indicate a relatively low-grade iron ore. Gold content reaches a maximum of 1.1 ppb. Low Al_2O_3, TiO_2 and High Field Strength Elements (HFSE) indicate BIF derivation from detritus-free chemical sediments. Their Fe/Ti, Fe/Al and Si/Al ratios are typical of marine BIF systems with hydrothermal overprint. On Post Archaean Australian Shale (PAAS)-normalized Rare Earth Elements-Yttrium (REE-Y) patterns the BIFs present a slightly negative Ce anomaly and positive Eu and Y anomalies; characteristics typical of modern seawater. The amphibolites are enriched in Light Rare Earth Elements (LREE) relative to Heavy Rare Earth Elements (HREE) and show peaks of Y, Nb, La Ta and their Au content attains a maximum of 1.7 ppm. Gold contents in the BIFs and amphibolites indicate the BIF-related country rocks as a potential primary source of the alluvial gold mined in the Mbalam district.

Key words: BIF, amphibolite, petrology, hydrothermal, seawater, Mbalam prospect, Cameroon.

Received: 12/08/2022

Accepted: 27/09/2022

DOI: https://dx.doi.org/10.4314/jcas.v182.5

RESUME

Les gisements de Fer rubanés (BIFs) localisés à la limite Nord du district ferrifere de Mbalam, sont partiellement représentatives des ceintures de roches vertes Archéennes à Protérozoïques dans le Craton du Congo (CC). Dans cette étude, la pétrologie des BIFs et amphibolites de la partie inferieure de la crête de Njweng est présentée afin de déceler la source des sédiments ainsi que leur enrichissement en Fer. Différentes catégories de BIFs variant des facies à oxydes aux silicates, sont composées principalement de bandes à magnétite avec alternances de bandes quartzeux. Leur minéralogie est dominée par la magnétite, l'hématite et le quartz. Les amphibolites contiennent du quartz, magnétite, l'amphibole, biotite, et grenat avec une schistosité distincte. La teneur en Fe_2O_3 et SiO_2 des BIFs atteint un maximum en poids de 54,55 % et 57,83 % respectivement. La teneur moyenne en Fe_2O_3 de 46,7 % en poids, associée au SiO_2 et Al_2O_3 comme éléments délétères, indique un minerai de fer à teneur relativement faible. Les teneurs en Or atteignent un maximum de 1,1 ppb. Les faibles teneurs en Al_2O_3, TiO_2 et élément de champ électrostatique élevé (HFSE) indiquent que les BIFs dérivent d'un environnement sédimentaire chimique d'origine non détritique. Leur rapports Fe/Ti, Fe/Al et Si/Al sont typiques des systèmes BIFs marin avec une signature hydrothermale. Sur les modèles tarres rares-yttrium normalisés par schiste australien post- archéen (PAAS), les BIFs révèlent une légère anomalie négative de Ce couplée à une anomalie positive de Eu et Y, caractéristique d'un environnement marin récent. Les amphibolites sont enrichies en tarres rares légères par rapport aux tarres rares lourdes et montrent des pics de Y, Nb, La et Ta, Leurs teneurs en Au atteignent un maximum de 1,7 ppm. Les teneurs en Or dans les BIFs et les amphibolites indiquent que les formations de fer rubanées (BIFs) en place dans le district de Mbalam sont une source potentielle d'or.

Mots clés: BIFs, amphibolites, pétrologie, hydrothermale, environnement marin, prospect de Mbalam, Cameroun.

1. INTRODUCTION

Banded iron formations (BIFs) are rock units with distinct alternations of Fe-rich and chert-rich bands (Kimberley, 1989). They typically vary in age from Archean (3.8 Ga) to Paleoproterozoic (2.5 Ga) and are thought to have formed from seawater as chemical precipitates. The total Fe content of BIFs falls between 20 wt% and 40 wt% and silica content ranges from 34 to 56 wt% (Klein, 2005). BIFs generally occur in greenstone belts and other super crustal volcanic and/or sedimentary sequences of deep marine environments and they range from oxide-, carbonate-, silicate- to sulfide-rich varieties. Precambrian BIFs represent an important source of mineable iron (Teutsong *et al.,* 2017). According to Suh *et al.* (2008) the high demand for steel worldwide is partly driven by an enormous economic growth currently underway in India and China. Consequently, the search for new iron deposits is experiencing an upsurge in Cameroon where Archean to Early Proterozoic BIF deposits are limited to the south and southeastern part of the country (Suh *et al.,* 2008; Chombong and Suh, 2013). This part of the country is at the northern edge of the Congo Craton (CC) where a new iron ore exploration belt has opened (Fig. 1) and has been the subject of recent publications (Ilouga *et al.,* 2013; Chombong *et al.,* 2013; Teutsong *et al.,* 2017; Ganno *et al.,* 2015, 2017; Chombong *et al.,* 2017, Soh *et al.,* 2018; Ndime *et al.,* 2018, 2019; Ndema *et al.,* 2020; Bonda *et al.,* 2022).

The last two decades have witnessed a boom in alluvial gold mining in the iron ore-bearing terrains of southern Cameroon. Understanding the nature of gold mineralization in this greenstone

metamorphic belt has been the focus of some recent studies (Fuanya *et al.,* 2019; Omang *et al.,* 2015; Dongmo *et al.,* 2019; Nono *et al.,* 2021), yet the primary source of gold mineralization is unknown. Previous studies are in favour of an ultramafic host for the primary mineralization (Omang *et al.,* 2015; Dongmo *et al.,* 2019; Fuanya *et al.,* 2019). Studies of gold deposits associated with BIFs in the Archean cratons have shown that gold is associated with localized sulfide facies zones within regionally extent oxide-facies units (Biczok *et al.,* 2012).

This study is aimed at characterizing the Fe-enriched rocks of part of the Mbalam district through detailed petrography and geochemical analysis of BIFs and associated host rocks. This data set should provide insights into their genesis and serve as a gate way to determine the primary gold host rock and thus enhance exploration in the area.

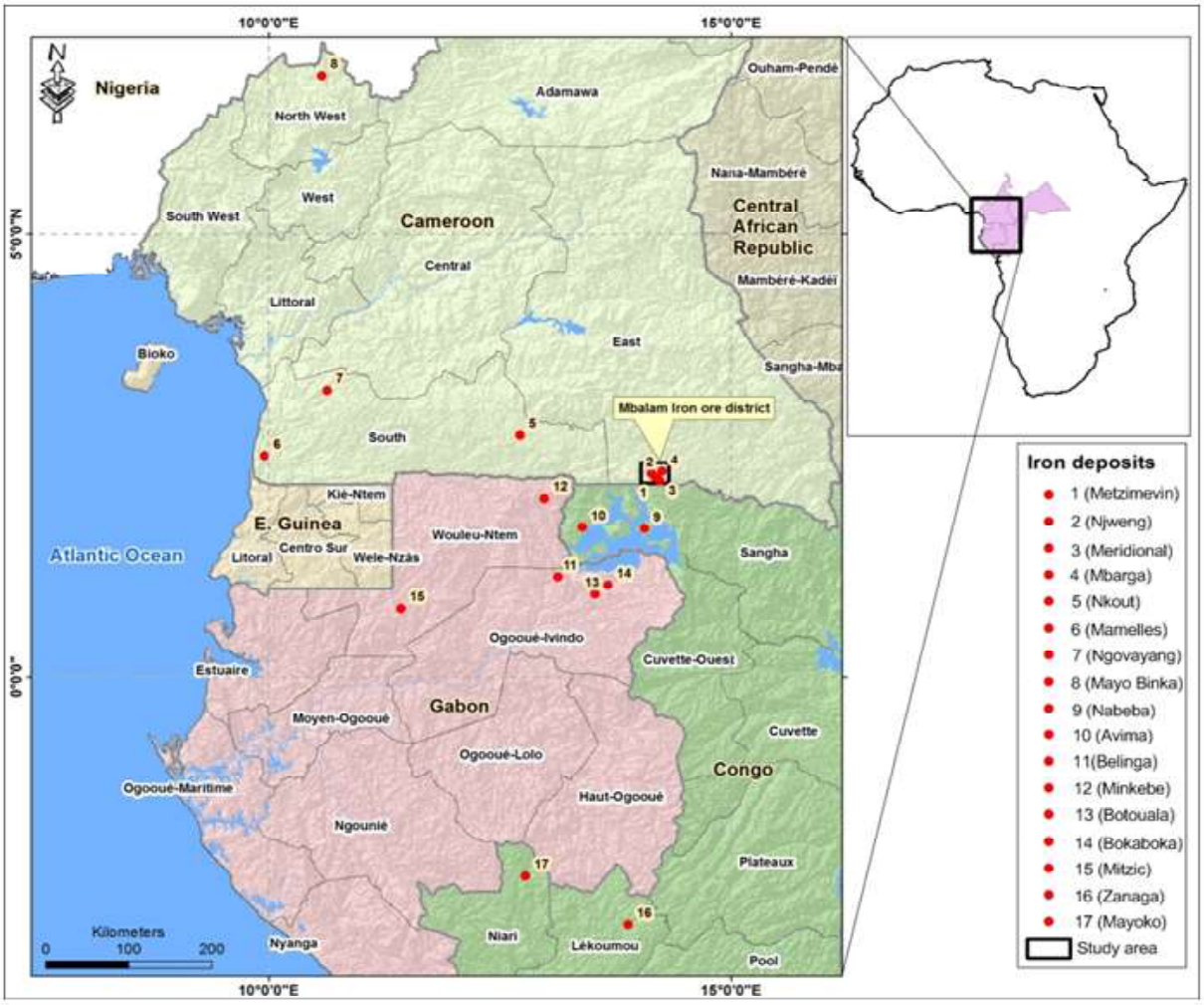

Fig. 1: New iron ore exploration belt in the northern part of the Congo Craton with iron ore deposits in Cameroon, Congo and Gabon

2. REGIONAL AND DISTRICT GEOLOGICAL ASPECTS

The Mbalam iron ore prospect constitutes a segment of the Ntem complex (Fig. 2, Ilouga *et al.,* 2013) which is part of the CC composed of Archean rocks (2.8 and 2.9 Ga) that appear to have been partially reworked during the Paleoproterozoic Trans Amazonian cycle (Shang *et al.,* 2004, 2007; Tchameni *et al.,* 2001; Van Schmus *et al.,* 2008; Chombong *et al.*, 2013, Chombong and Suh, 2013, Li *et al.,* 2016). The magmatic rocks here include charnockitic and

TTG (Tonalite-Trondjemite-Granodiorite) suites (Pouclet *et al.,* 2007) and the granitoids are mainly I-type (Shang *et al.,* 2004). The banded series is represented by highly deformed granulitic gneisses (Takam *et al.,* 2009) while the greenstone rocks occur as disrupted belts and as xenoliths in the intrusive series (Shang *et al.,* 2004, 2007). These supracrustal rocks consist of BIFs, metagraywackes, sillimanite-bearing paragneisses, amphibolites and pyroxenites affected by granulite-facies metamorphism with estimated peak temperatures of 750 ± 50 °C at 5–6 kbar (Tchameni *et al.,* 2001). Rock units of economic importance in the Ntem complex include high-grade iron ore and itabirites (Suh *et al.,* 2008; Ilouga *et al.,* 2013; Ndime *et al.,* 2019) with less prominent ultrabasic rocks containing elevated Ni, Cr and Co (Milesi *et al.,* 2006). Polyphase deformation in the Ntem complex is revealed by the prominent E-W-trending foliation truncated by late NE-SW shear zones adorned with late felsic plutons.

The Njweng prospect is a ridge trending N-S with a surface area of ~ 80 km^2. It is 7 km long and constitutes one of the four ridges of the Mbalam iron ore district (Fig. 3). The BIF is hundreds of meters thick (more than 600 m in depth), with maiden resources of approximately 3.5 Mt of iron at Mbarga the main ridge of the district (www.sundanceresources.com.au). The prospect is composed predominantly of metamorphosed chemical sediments (Ilouga *et al.,* 2013). Associated supracrustal rocks consist of matagranitoids and amphibolites. The BIF is intercalated with metasandstone and metasiltstone with variable ages from 1000-3000 Ma (Chombong *et al.,* 2013). Structurally the first deformation event in the area involved regional E-W shortening. This resulted in a dominant isoclinal recumbent F1 fold with the early N-verging, overprinted by a late W-verging open F2 fold expressed in the itabirite. The itabirite bands have N-S strike with a near vertical dip (average 75°), and a dip direction that varies between E and W.

3. MATERIAL AND METHODS

During field mapping for this study of the southern end of the Njweng ridge previously documented by Ilouga *et al.* (2013), rock samples were collected preferably in the vicinity of alluvial gold workings as the desire was to pinpoint potential gold source rocks. Eight representative BIF and amphibolites samples were subsequently selected for petrography and geochemical analysis. Samples collected were grouped into facies based on their mineralogy, texture and field distribution and subsequently thin sections prepared from them were studied under a petrographic microscope.

Whole rock geochemical analysis was achieved at Acme Analytical Laboratories Ltd., Vancouver, Canada using a combination of inductively coupled plasma emission spectrometry (ICP-ES) and mass spectrometry (ICP-MS). A 0.2 g of pulverized sample was fused using lithium metaborate/tetraborate and digested using dilute nitric acid. Loss on ignition was determined by weight difference after ignition at 1000°C. In addition, a separate 0.5 g split was digested in aqua regia and analyzed by ICP-MS for precious and base metals. The major elements were analyzed by ICP-ES while total C and S was determined by Leco. Trace, REE as well as the precious and base metals were analyzed by ICP-MS. In order to ensure data quality and to calibrate the equipment for optimal precision, a replicate, standard (STD SO-18) and blank was run after every sample analyzed. Accuracy for major, trace and rare earth element (REE) analyses was within 5% error margin. The detection limits for the major elements vary between 0.002 and 0.01 wt%, 0.05 to 1 ppm for trace and REE elements and 0.01 to 1 ppm for precious and base metals.

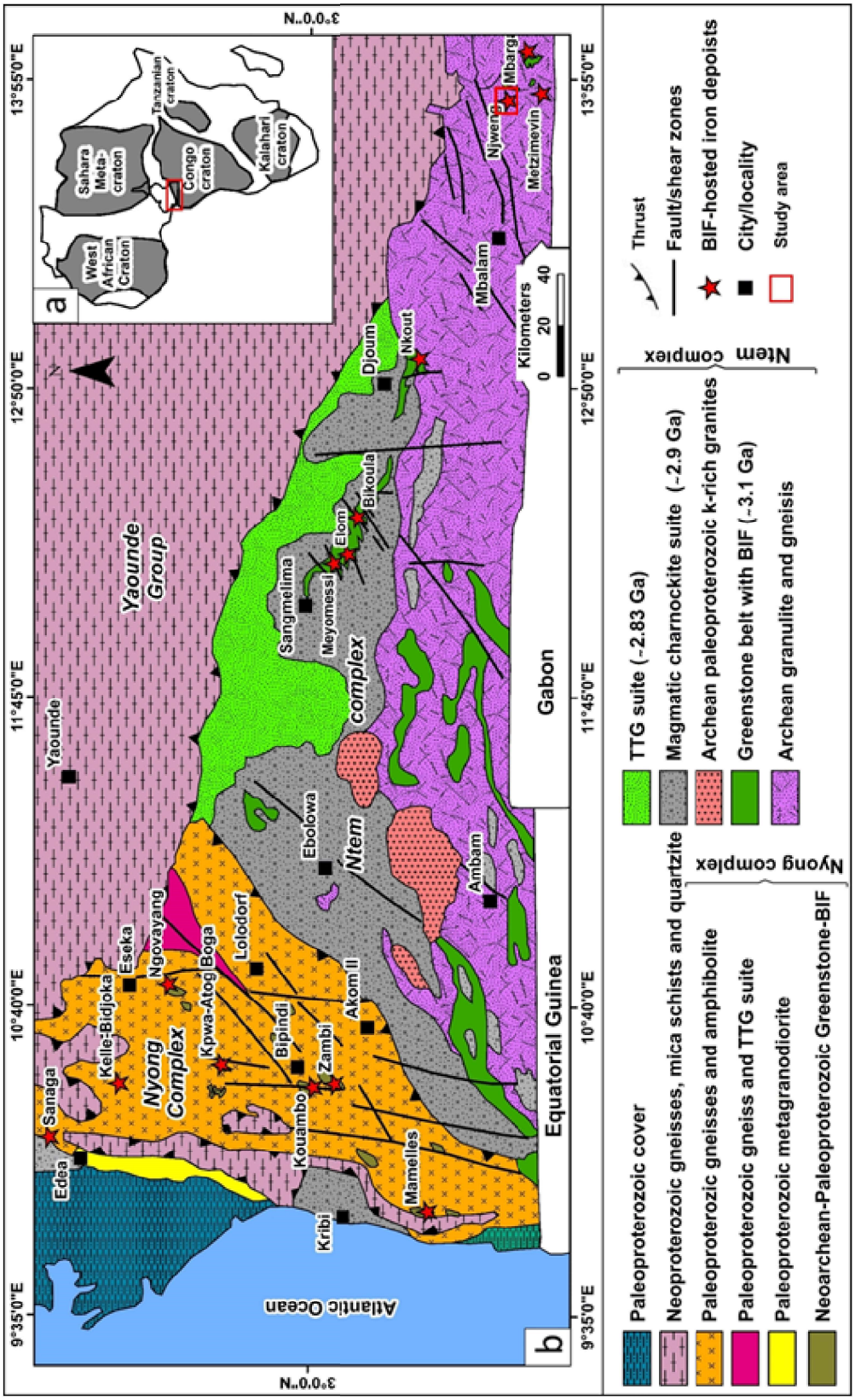

Fig. 2: Regional geologic map of southern Cameroon indicating the location of the Njweng prospect within the Mbalam iron ore district. The Mbalam iron ore district is part of the Ntem complex in the northern limit of the Congo craton.

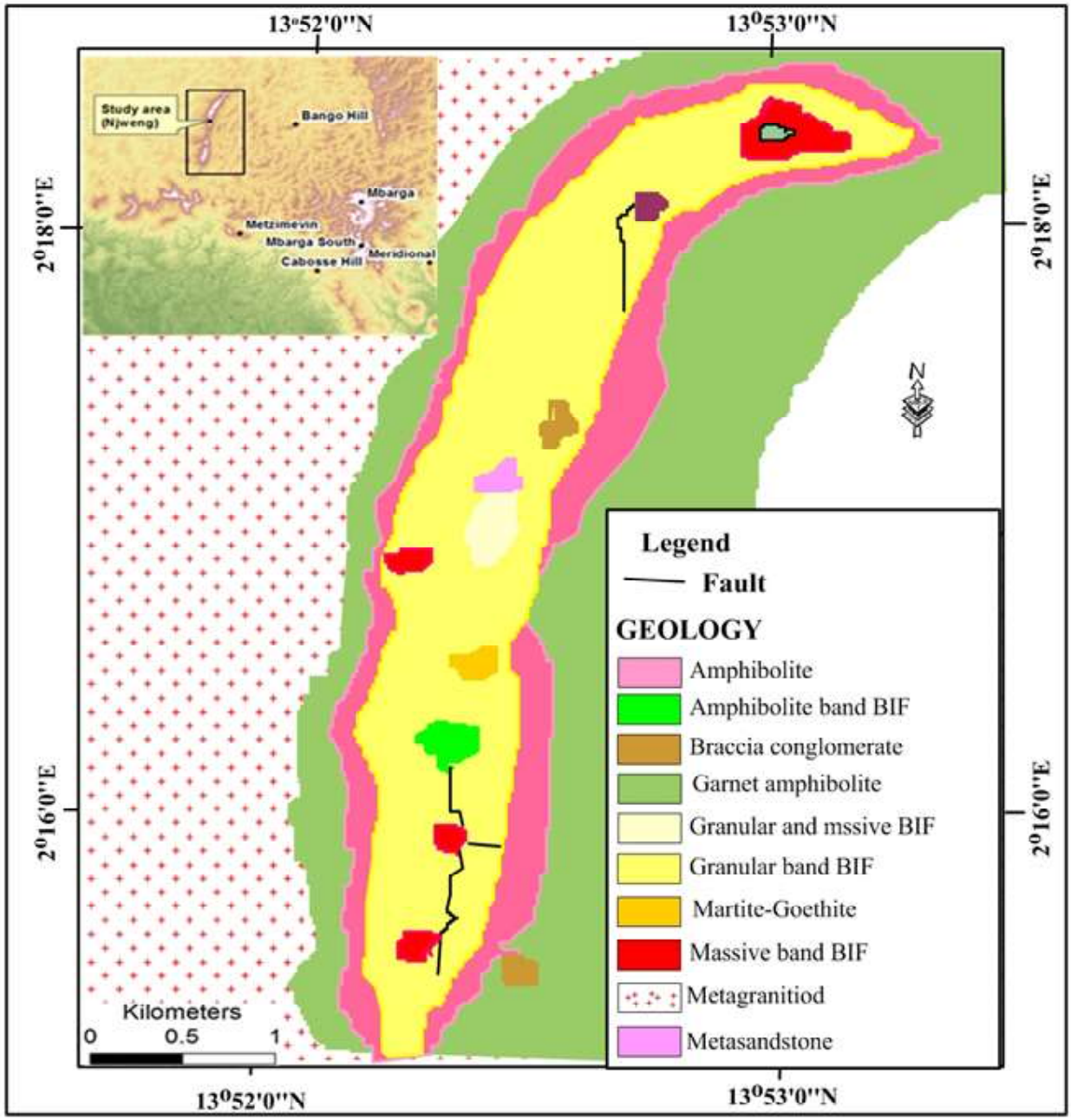

Fig. 3: Geology of the Njweng prospect mordified from Ilouga *et al.,* 2013.

4. RESULTS

4.1. Petrographic characteristics of BIFs and amphibolites from the Njweng area

4.1.1. Banded iron formation

Two types of BIF have been distinguished based on their mineralogy, namely the oxide and the silicate facies BIF.

The oxide facies BIF is marked by distinct alternation of the iron-rich bands that vary in thickness from 1 to 3 mm and silica-rich bands with thicknesses that range from 2 to 5 mm (Fig. 4a, b). In some cases, the bands are folded (Fig. 4) and granular to massive. The iron-rich band is composed of iron oxides (magnetite with minor hematite). Magnetite crystals occur as large subhedral to anhedral grains dominantly showing a granoblastic texture with inclusions of quartz (Fig. 5). Some magnetite grains are oxidized to hematite around their rims (Fig. 5). The silica-rich bands are mainly composed of quartz with disseminations of magnetite crystals. Quartz is medium to coarse-grained, subhedral to anhedral in shape and exhibits undulose extinction.

The silicate facies BIFs is essentially composed of quartz that is sparingly stained by hematite (Fig. 4). The silicate facies BIF samples show alternating silica- and Fe-rich bands some of which are weakly to strongly folded (Fig. 4). While the silica-rich bands vary in thickness from 3 to 9 mm, the iron-rich bands reveal thicknesses that range from 1 to 4 mm. The main iron oxide in the silicate facies is magnetite with a vesicular texture (Fig. 5).

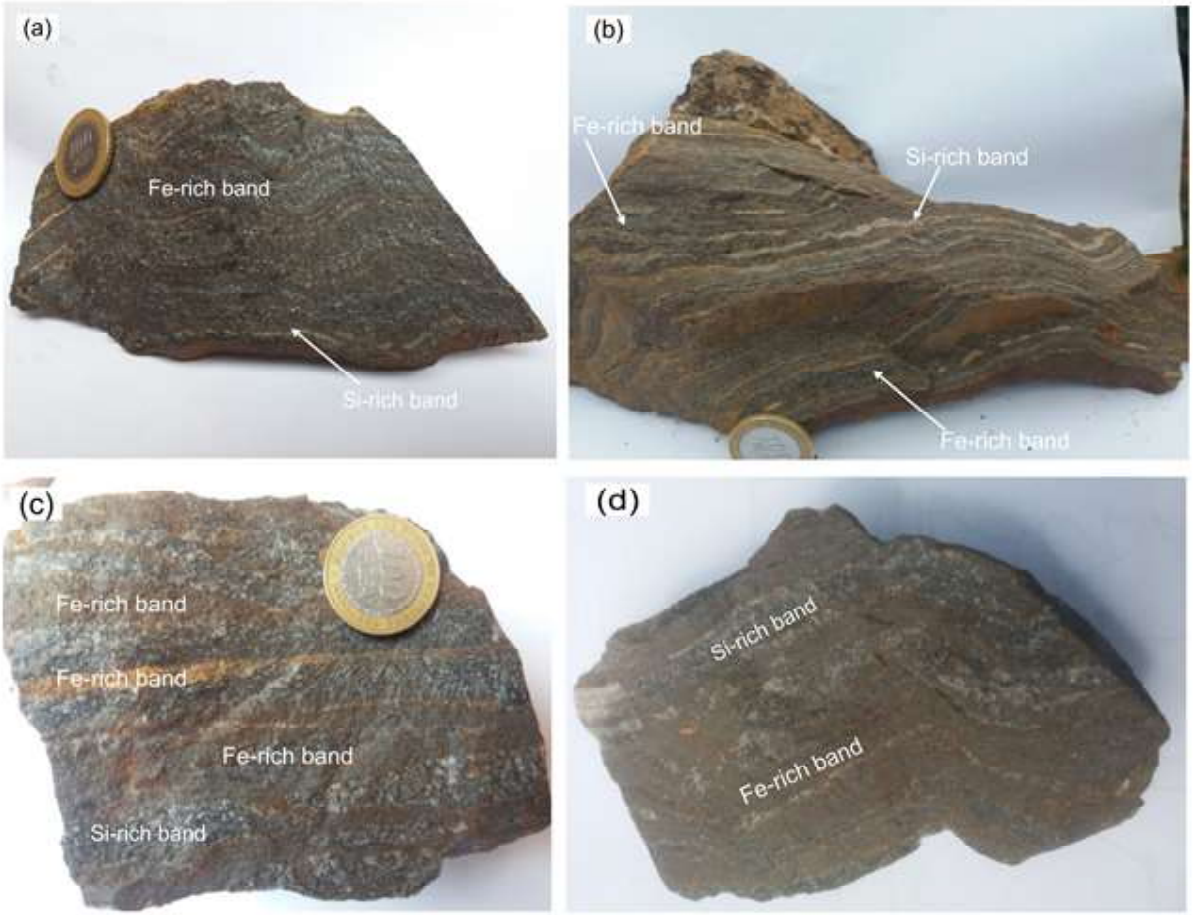

Fig. 4: Hand specimen samples of the oxide and silicate facies BIFs from the Njweng prospect. (a, b) Characteristic oxide-facies BIF showing alternating Fe-rich and Si-rich bands. The bands vary from granular to massive. (c) Silicate facies BIF showing alternating iron and silica bands. Fe-band which are yellow in color indicated oxidation. (d) BIF indicting a characteristic folded structure.

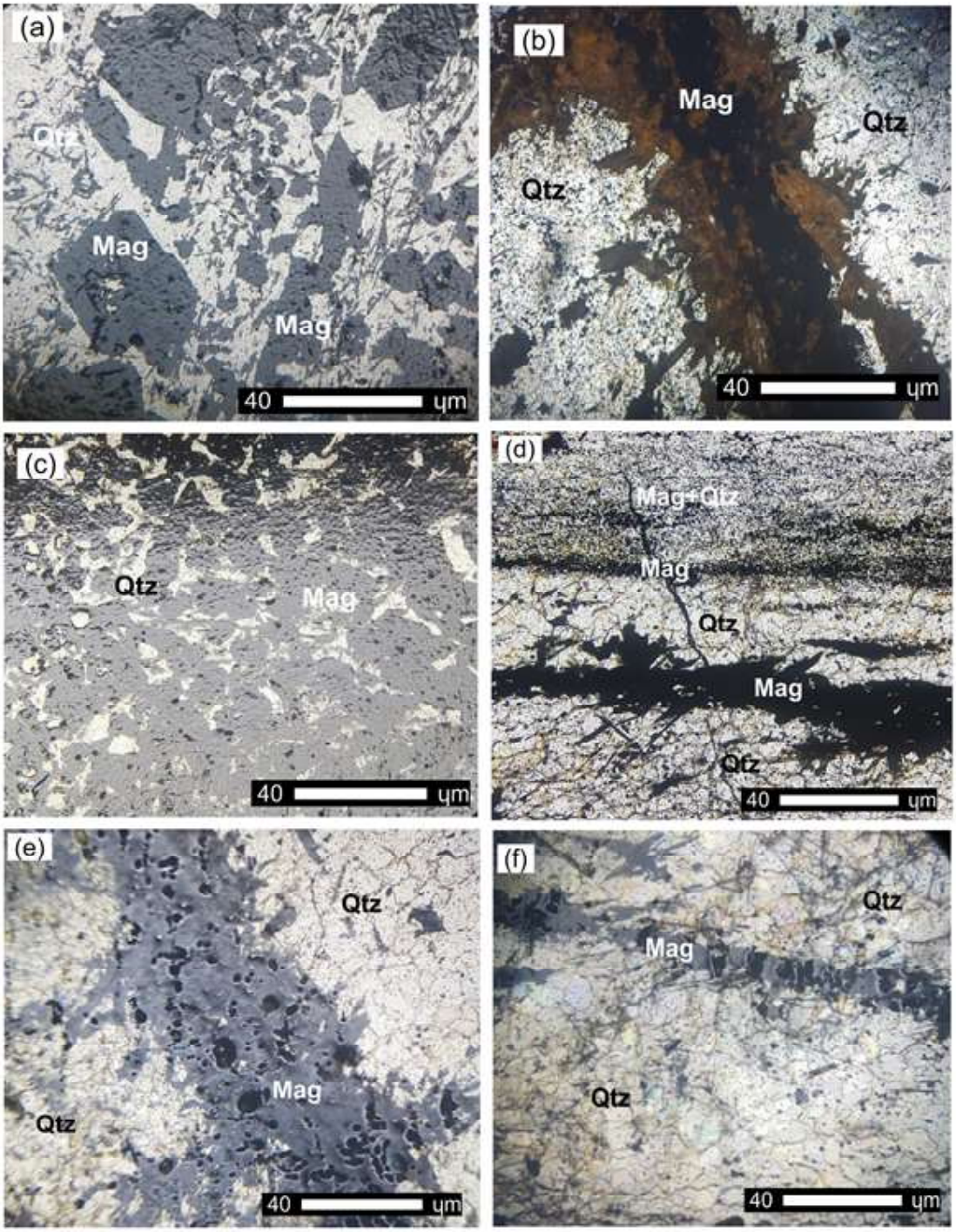

Fig. 5: Photomicrographs of the oxide and silicate facie BIF as observe under reflected light. (a, b) Heteroblastic texture with silica occurring as inclusions in magnetite. Note discontinuous magnetite and silica bands. (c) Magnetite oxidized to hematite. Notice the reddish brown color. (d) Magnetite band showing granublastic texture with silica inclusions. Alternating bands of magnetite and quartz. Magnetite is vesicular while quartz shows a characteristic coarse texture. Notice a magnetite vein-let that cuts across both the magnetite and the silica bands (e, f). Vesicular texture in magnetite. Abbreviations Mag=magnetite, qtz=quartz.

4.1.2. Amphibolite

The amphibolites are dark green, foliated and medium- to coarse-grained (Fig. 6). Two varieties have been distinguished based on their mineralogy: garnet-bearing and non-garnet types. The garnet-bearing amphibolite has an equigranular to granoblastic texture (Fig. 6) with platy and elongated aligned amphibole grains (Fig. 7) coupled with garnet, biotite, hornblende and quartz. Garnet porphyroblasts (0.23 - 1 mm) are subhedral and show characteristic irregular fractures (Fig. 7a). Hornblende is subhedral and needle-like to elongate in shape (Fig. 7a, b). Two quartz types have been identified herein referred to as qtz1 and qtz2. While qtz1 is fine-grained and makes up the groundmass, qtz2 is coarse-grained and occurs both in veinlets and in the groundmass of the rock (Fig. 7a-c). Quartz shows a characteristic ribbon texture and wavy extinction. The non-garnet amphibolite variety is granoblastic to heteroblastic and occurs in direct contact with the BIFs. Minerals identified include amphiboles (notably hornblende), quartz and magnetite (Fig. 7d-f). The schistosity here is defined by the preferred alignment of the amphiboles (Fig. 7d-f) which are poikiloblastic with quartz inclusions (Fig. 7d). The amphiboles are altered to chlorite to a limited extent. Quartz occurs as ribbons and shows characteristic undulose extinction. Magnetite occurs as disseminations along the cleavages of the amphiboles.

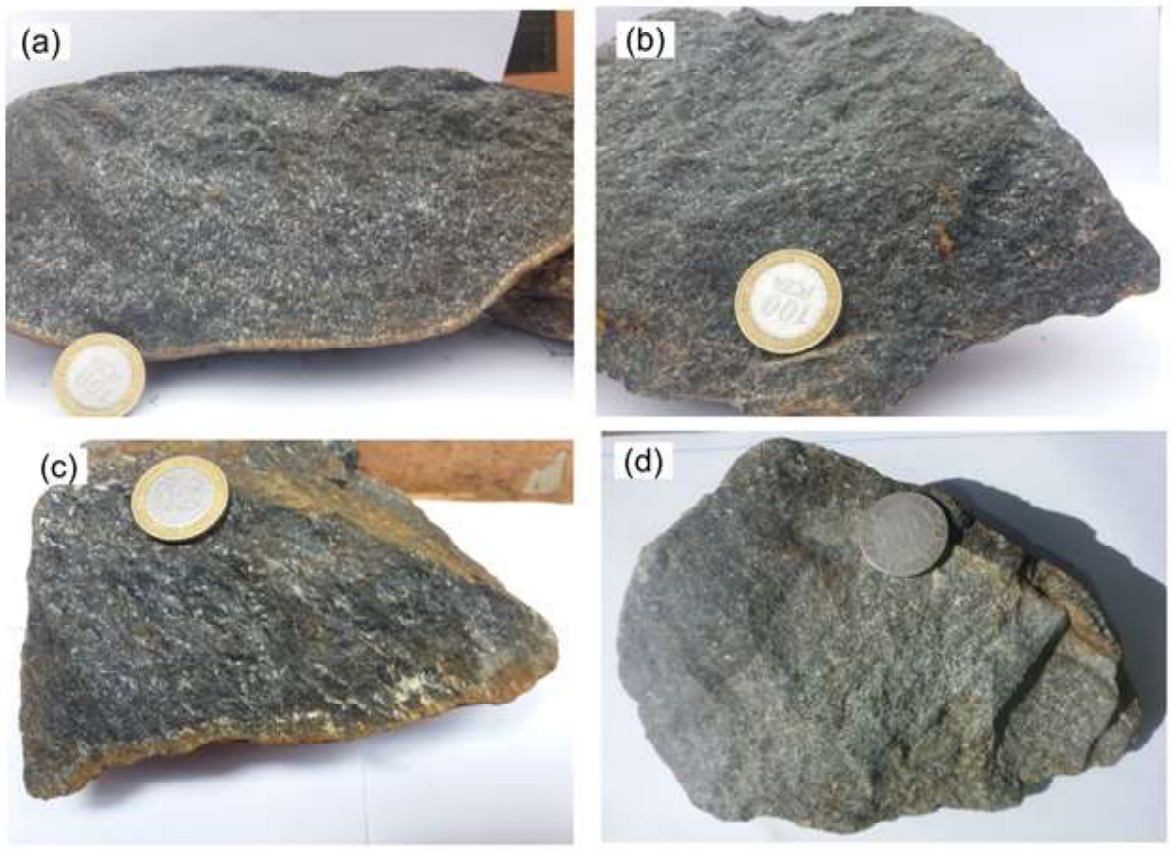

Fig. 6: (a) Amphibolite showing medium grain granular texture with minerals such as amphiboles (hornblende), quartz and accessory sulphide (b) Coarse grain amphibolite, pinkish in color with amphiboles, and quartz (c) Coarse grain amphibolite with schistocity define by preferred alignment of amphiboles minerals. (d) Garnet bearing amphibolites showing a medium to coarse-grained textures.

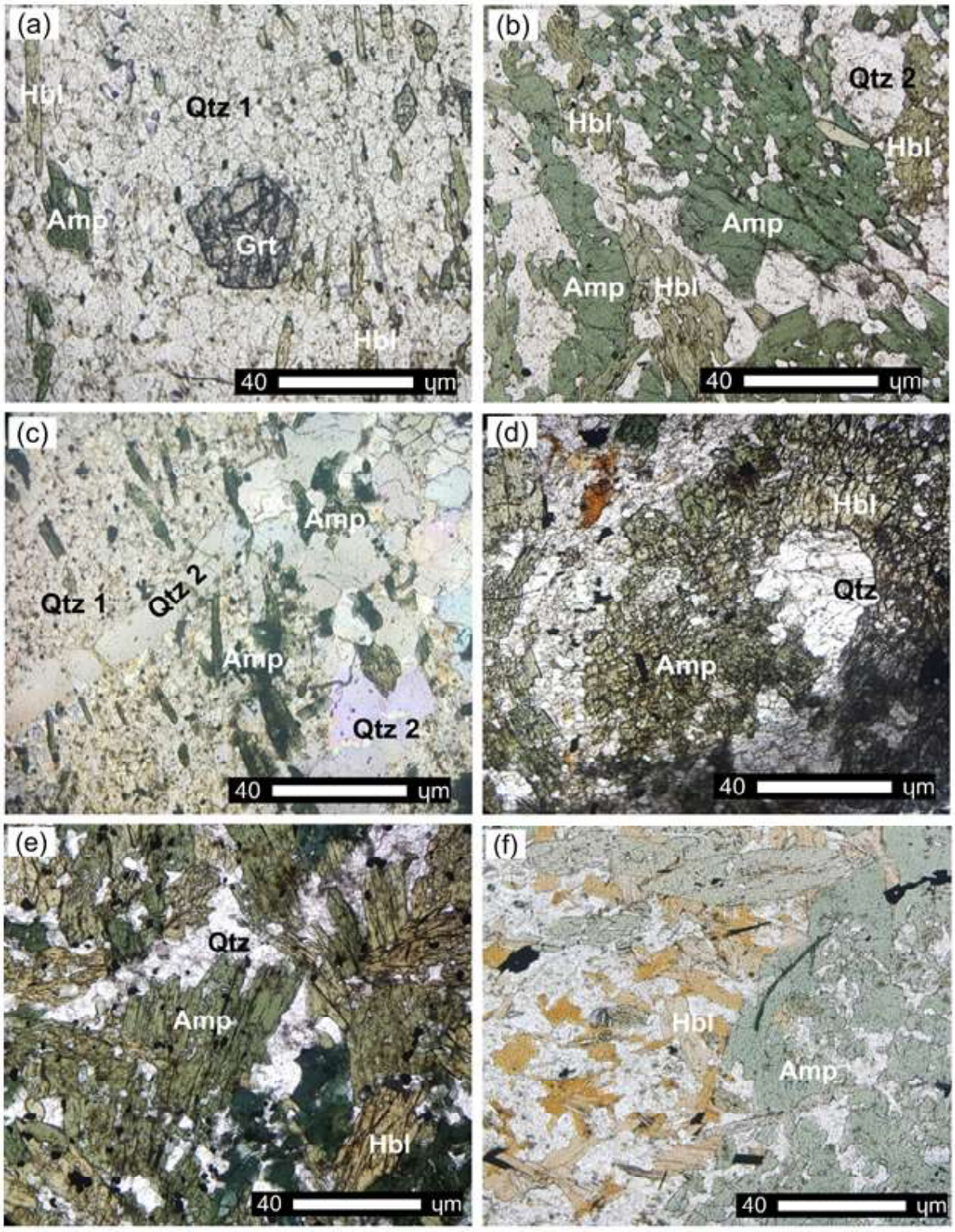

Fig. 7: Photomicrographs of garnet bearing amphibolite taken under plane polarized light and crossed nicoles. Samples a,b,c represents garnet bearing amphibolites while d,e,f represents non garnet bearing amphibolites. (a) Coarse-grained garnet bearing amphibolites, with hornblende, amphiboles, quartz, biotite and feldspar (b) Coarse-grained amphiboles and hornblende in a groundmass of quartz and feldspar. The amphiboles show a preferred orientation. (c) Quartz ribbons perpendicular to the general orientation of the amphiboles. Notice both the quartz 1 and quartz 2. (d) Amphibole (Amp) with, quartz, biotite and

opaque minerals mineral association. (e) Coarse-grained euhedral to subhedral hornblende and amphibole crystal in a groundmass of biotite and quartz. (f) Coarse-grained euhedral to subhedral hornblende and amphibole crystal in a groundmass of quartz. Abbreviations grt=garnet, hbl=hornblend, amp=amphibole, qtz=quartz, bt=biotite, fsp=feldspar, opq=opaque minerals

4.2. Whole rock geochemistry

The whole rock geochemical data of the BIFs and amphibolites are presented in Table 1. The BIFs reveal $Fe_2O_{3\,(T)}$ and SiO_2 contents that range from 38.39 to 54.55 wt% in the silicate and oxide facies, respectively. Their SiO_2 contents vary between 42.12 and 57.82 wt%. Deleterious elements such as Al_2O_3, P_2O_5, and TiO_2, are generally low (Table 1). Besides Co, W and Zn with concentrations that reach a maximum of 178.9 ppm Co, 1742.4 ppm W and 24 ppm Zn, the concentrations of trace elements in the BIFs are low. Gold content attains a maximum of 1.1 ppb. The BIFs are hydrothermal in origin (Fig. 8a) with formation temperatures that vary between 200-300°C (Fig. 8b). REE and Y abundances of the BIFs are listed in Table 1 and REEY data are illustrated in Post-Archean Australian shale (PAAS)-normalized REE diagrams (Fig. 9a). The total REEY concentrations (ÓREEY) of all the samples range from 19.15 to 28.50. PAAS-normalized REE patterns of the BIFs are characterized by a depletion in LREE (La/Yb_{SN}= <1) compared to the HREE. This is coupled with a slightly negative Ce and positive Eu (Eu/Eu*, 2.7) and Y anomalies (Y/Y*, 1 to 1.3, Table 1, Fig. 9b). On the $(Ce/Ce^*)_{SN}$ vs. $(Pr/Pr^*)_{SN}$ diagram (after Bau and Dulski, 1996) the BIF samples plot within the category IIa field (Fig. 11). They show Gd_{SN}/Gd_{SN}* values that vary between 1.0 and 1.1, redox-sensitive Ce_{SN}/Ce_{SN}* values that range from 0.72 to 0.98 and a slightly super chondritic Y/Ho ratio from 27.8 to 33.5 (Table 1).

The SiO_2 content of the amphibolites ranges from 47.68 wt% to 53.34 wt% (Table 1). The concentration of Al_2O_3 varies from 0.03 to 14.04 wt%. The sum of the alkali ($Na_2O + K_2O$) ranges from 0.43 to 2.58 ppm. Their $Fe_2O_{3(T)}$ content ranges from 12.74 to 47.51 wt% (Table 1). The amphibolites show high concentrations of Ba, Co, Cu, Ni, Rb, Sc, Sr V, W, Zn and Zr. This is coupled with an elevated content of Au (1.7 ppb). REE and Y abundances (REEY) of the amphibolites are listed in Table 1 and REEY data are illustrated on C1 Chondrite-normalized REE diagrams (Fig. 10a). The total REE and Y concentrations (ÓREEY) of all the samples range from 11.6 to 75.89. C1 chondrite normalized REE patterns of the amphibolites are characterized by a slight enrichment in LREE (La/Yb_{sn}= >1) coupled with a variation in the Eu (Eu/Eu*, 0.9 to 1.9) and Y anomalies (Y/Y*, 0.9 to 1.3, Table 1, Fig. 10a). The samples also show Gd_{SN}/Gd_{SN}* values that vary between 0.9 and 1.2, redox-sensitive Ce_{SN}/Ce_{SN}* values that range from 0.4 to 0.9 and Y/Ho ratios from 25.6 to 38.18 (Table 1). On multi-element variation diagrams the amphibolites show peaks of Y, Nb, La and Ta. They are also characterized by troughs in Rb, Cs and Pb (Fig. 10b).

Table 1: Major, trace and REE composition of BIFs and amphibolites sampled from the Njweng ridge, Southern Cameroon

	Sample	NG01	NG06	NG03	NG04	NG07	NG08
		siliceous BIF	Oxide BIF	Amphibolite	Amphibolite	Amphibolite	Amphibolite
wt%	DL						
SiO_2	0.01	57.82	42.12	53.34	50.75	47.68	47.83
Al_2O_3	0.01	0.04	0.03	8.83	0.03	0.03	16.04
Fe_2O_3	0.04	38.39	54.55	23.69	45.19	47.51	12.74
MgO	0.01	bdl	0.03	5.68	bdl	2.59	9.12
CaO	0.01	bdl	bdl	6.16	bdl	0.94	8.86
Na_2O	0.01	bdl	bdl	0.37	bdl	bdl	1.98
K_2O	0.01	bdl	bdl	0.06	bdl	bdl	0.60
TiO_2	0.01	bdl	bdl	0.51	bdl	bdl	0.58
P_2O_5	0.01	0.11	0.22	0.11	0.11	0.23	0.08
MnO	0.01	bdl	0.04	0.23	0.01	0.09	0.18
Cr_2O_3	0.002	bdl	bdl	0.092	bdl	bdl	0.012
LOI	-5.1	3.4	2.8	0.6	3.4	0.7	1.7
Sum	0.01	99.74	99.78	99.68	99.53	99.76	99.71
TOT/C	0.02	0.04	0.04	0.03	0.04	0.03	0.04
TOT/S	0.02	bdl	bdl	1.02	bdl	bdl	0.06
Au ppb	0.5	1.0	1.1	1.7	bdl	0.7	0.8
Ag ppm	0.1	bdl	bdl	bdl	bdl	bdl	bdl
As	0.5	bdl	bdl	bdl	bdl	bdl	bdl
Ba	1	3	3	5	bdl	3	157
Be	1	bdl	1	bdl	bdl	bdl	1
Bi	0.1	bdl	bdl	0.2	bdl	bdl	bdl
Cd	0.1	bdl	bdl	bdl	bdl	bdl	bdl
Co	0.2	178.9	143.6	130.7	271.9	135.6	97.6
Cs	0.1	bdl	bdl	bdl	bdl	bdl	0.9
Cu	0.1	2.4	1.4	163.4	1.7	0.9	38.1
Ga	0.5	bdl	bdl	11.0	bdl	bdl	12.4
Hf	0.1	bdl	bdl	1.2	bdl	bdl	1.6
Hg	0.01	bdl	bdl	bdl	bdl	bdl	bdl
Mo	0.1	2.3	1.8	1.5	3.4	1.6	0.8
Nb	0.1	0.3	0.3	2.3	0.3	0.5	2.4
Ni	0.1	4.4	2.0	275.3	8.2	2.5	44.6
Pb	0.1	0.5	bdl	0.4	bdl	bdl	3.0
Rb	0.1	0.3	bdl	0.4	0.2	bdl	20.6
Sb	0.1	bdl	bdl	bdl	0.1	bdl	bdl
Sc	1	bdl	2	24	2	1	40
Se	0.5	bdl	bdl	1.0	bdl	bdl	bdl
Sn	1	bdl	bdl	bdl	bdl	bdl	bdl
Sr	0.5	bdl	bdl	38.4	bdl	1.6	110.0

Table 1 Continued

	Sample	NG01 Siliceous BIF	NG06 Oxide BIF	NG03 Amphibolite	NG04 Amphibolite	NG07 Amphibolite	NG08 Amphibolite
ppm	MDL						
Ta	0.1	3.0	2.6	1.8	5.5	2.9	0.7
Th	0.2	bdl	bdl	0.8	bdl	bdl	0.2
Tl	0.1	bdl	bdl	bdl	bdl	bdl	bdl
U	0.1	bdl	bdl	0.2	bdl	bdl	bdl
V	8	bdl	bdl	169	bdl	bdl	209
W	0.5	1742.4	1652.6	958.5	2912.5	1586.0	377.0
Zn	1	4	24	14	6	40	23
Zr	0.1	1.1	0.9	38.7	0.7	0.8	57.9
Ppm							
La	0.1	6.2	2.6	4.4	1.4	1.8	10.4
Ce	0.1	9.5	3.9	9.7	2.3	3.4	9.6
Pr	0.02	1.06	0.60	1.28	0.28	0.44	3.12
Nd	0.3	4.0	2.7	5.4	1.2	2.3	13.9
Sm	0.05	0.71	0.52	1.36	0.24	0.43	3.18
Eu	0.02	0.40	0.33	0.47	0.20	0.29	1.16
Gd	0.05	0.68	0.66	1.79	0.40	0.56	3.61
Tb	0.01	0.10	0.12	0.31	0.06	0.10	0.63
Dy	0.05	0.68	0.70	1.93	0.48	0.67	3.52
Y	0.1	3.9	5.7	11.6	4.2	5.7	20.0
Ho	0.02	0.14	0.17	0.41	0.11	0.15	0.78
Er	0.03	0.45	0.52	1.23	0.34	0.46	2.47
Tm	0.01	0.08	0.08	0.17	0.05	0.07	0.41
Yb	0.05	0.52	0.48	1.12	0.29	0.40	2.69
Lu	0.01	0.08	0.07	0.17	0.05	0.07	0.42
Eu/Sm		0.56	0.63	0.35	0.83	0.67	0.36
Sm/Yb		1.36	1.08	1.21	0.83	1.08	1.18
Y/Ho		27.86	33.5	28.29	38.18	38	25.64
Y/Ho_{SN}		1.02	1.23	1.02	1.38	1.37	0.92
La/Yb_{SN}		0.88	0.40	2.82	3.46	3.23	2.77
La/Sm_{SN}		1.27	0.73	2.09	3.77	2.70	2.11
Gd/Yb_{SN}		0.79	0.83	1.32	1.14	1.16	1.11
La/Lu_{SN}		0.88	0.42	2.77	3.00	2.76	2.65
Tb/Yb_{SN}		0.70	0.91	1.26	0.94	1.16	1.06
$(Sm)_N*(Gd)_{SN}$		0.14	0.12	8.80	1.75	2.77	19.11
$Eu/Eu*_{SN}$		2.71	2.65	0.92	1.97	1.81	1.05
$(Sm/Yb)_{SN}$		0.99	0.73	3.32	0.59	1.05	7.77
$(Eu/Sm)_{SN}$		2.89	3.26	0.91	2.20	1.78	0.96
Ce/Ce*		0.85	0.72	0.98	0.85	0.91	0.41
Pr/Pr*		1.01	1.06	0.98	0.93	0.88	1.45

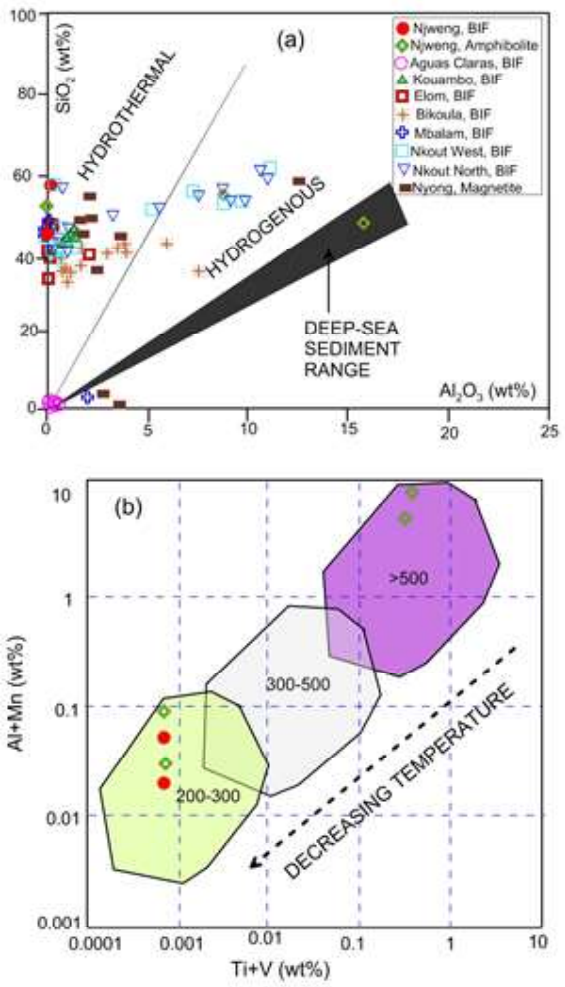

Fig. 8a): SiO_2 vs Al_2O_3 discrimination diagram after Choi and Hariya, 1992 indicating a hydrothermal affinity of the BIF. The amphibolites show hydrothermal, hydrogenous and deep-sea sediment compositions. (b) The Ti + V vs. Al + Mn diagram (Nadoll *et al.,* 2014) of BIF and amphibolite sampled from Njweng displaying a decreasing temperature trend. Note that these temperatures are estimates based on published values. The BIF is compared with BIF from classical deposits around the world Aguas Claras in Brazil (Spier *et al.,* 2007), BIF occurrences in Cameroon examples Kouambo BIF (Ganno *et al.,* 2017); Elom BIF (Ganno *et al.,* 2015); Bikoula BIF (Teutsong *et al.,* 2017); Nkout North and Nkout west BIF (Ndime *et al.,* 2018; 2019); Mballam BIF (Ilouga *et al.,* 2013) and Iron ore (magnetite) formations from the Nyong Unit (Chombong *et al.,* 2017).

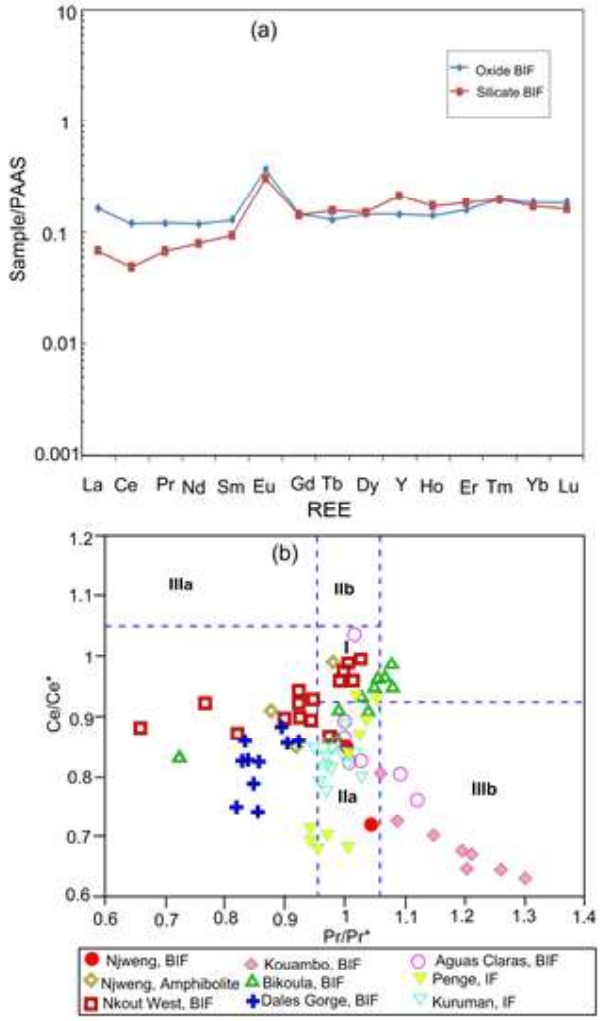

Fig. 9: (a) REE patterns (PAAS- normalized REE) of Njweng BIF. Normalization value of PAAS after McLennan, 1989. (b) $(Ce/Ce^*)_{SN}$ vs. $(Pr/Pr^*)_{SN}$ diagram (after Bau and Dulski, 1996) for the Njweng BIF. Field I: neither Ce nor La anomaly; field IIa: positive La anomaly, no Ce anomaly; field IIb: negative La anomaly, no Ce anomaly; field IIIa: positive Ce anomaly; field IIIb: negative Ce anomaly.

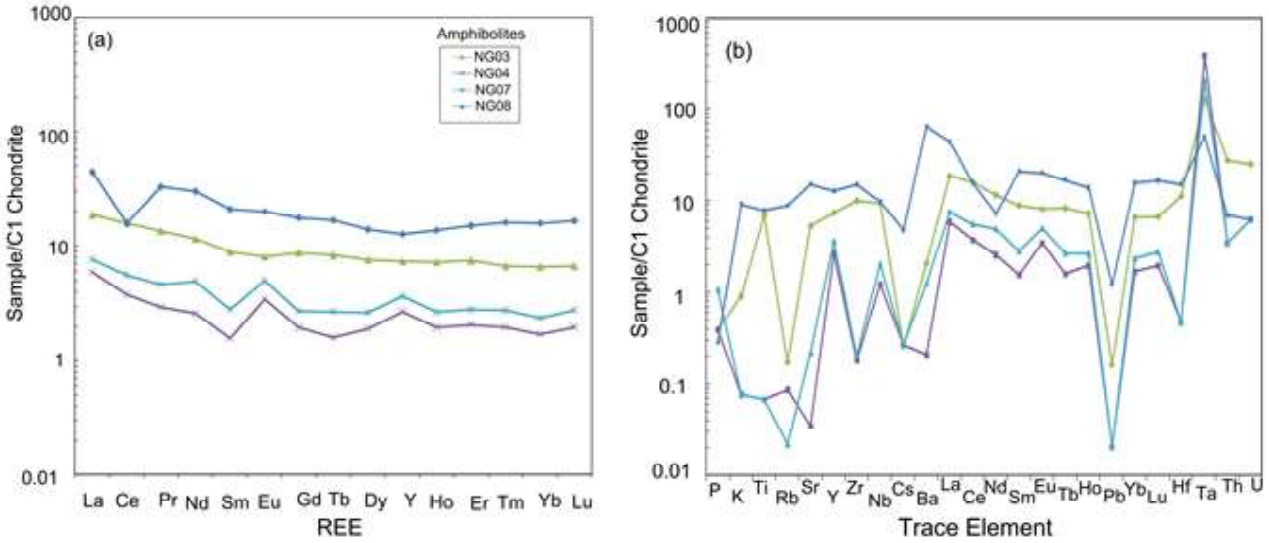

Fig. 10: REE and multi-element variation patterns (Chondrite-normalized REE) of amphibolites from Njweng. Normalization value of C1 Chondrite after Sun and McDonough, 1989.

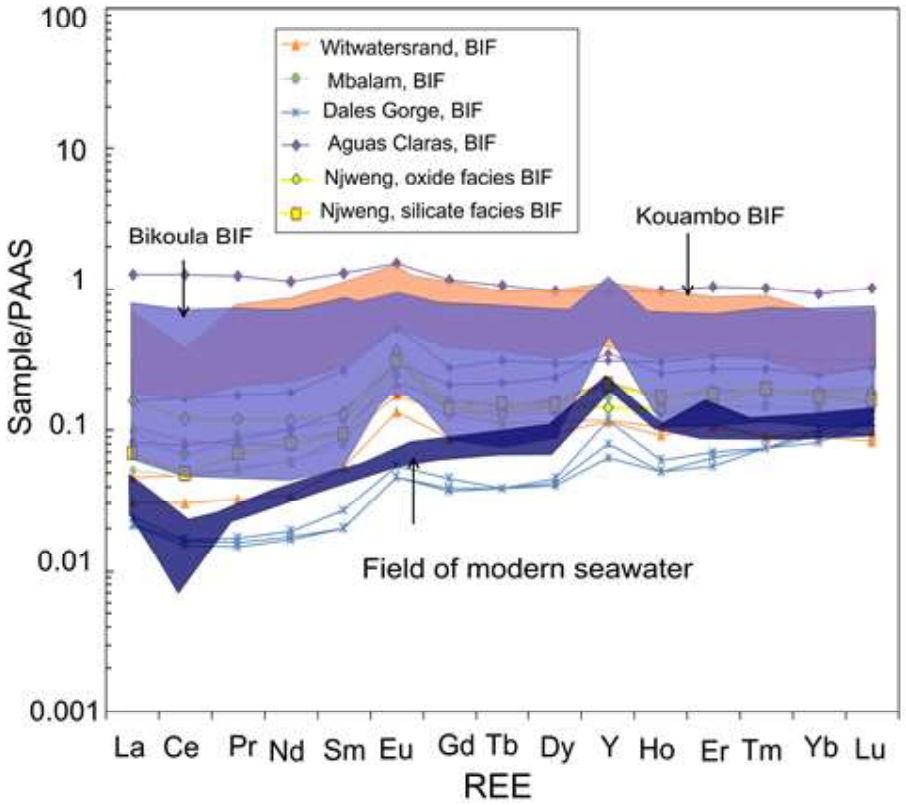

Fig. 11: Rare earth element pattern of BIF from the Njweng prospect compared with typical BIF from Cameroon (Ilouga *et al.,* 2013), Brazil (Spier *et al.,* 2008), South Africa (Viehmann *et al.,* 2015b) and Australia (Pecoits *et al.,* 2009). The samples are normalized to Post Archean Australian Shale (PAAS) after McLennan, 1989.

5. DISCUSSION

5.1. Mineralogical and textural characteristics of BIFs and associated country rocks

Millimetric bands of silica and iron oxides represent the only sedimentary features in the BIFs. Their fine lamination (microbanding) is interpreted to represent chemical valves or annual layers of sedimentation (Klein, 2005). Magnetite is the main iron oxide with hematite as a product of alteration. This is similar to magnetite reported by Suh *et al.* (2009) in the Metzimevin and Mbalam iron ore prospects. In the Aguas Claras and Matuca BIF deposits of the Quadrilatero Ferrifero in Brazil the principal iron oxide is heamatite (Spier *et al.,* 2008). This is in contrast to other Archean and Early Proterozoic BIFs with essentially magnetite as the main Fe-oxide mineral (Carlut *et al.,* 2015).

Magnetite is coarse-grained and granular to massive in texture with characteristic voids and inter-granular triple junctions. While the granular texture can be attributed to deposition in a shallow marine environment, the vuggy and massive texture represents leaching of gangue minerals by hypogene processes (Angerer and Hagemann, 2010; Duuring and Hagemann, 2013). Characteristic subhedral quartz inclusions in the magnetite are suggestive of metamorphic recrystallization (Ilouga *et al.,* 2013; Ndime *et al.,* 2019). The shape of the magnetite and quartz grains is a product of post-depositional recrystallization.

The amphibolites vary from granoblastic to heteroblastic with preferred mineral orientation, indicative of mineral recrystallization. They are characterized by amphibolites facies mineral assemblage, made up of quartz, magnetite, garnet, amphibole and biotite. Similar mineral assemblages have been reported by Ndime *et al.* (2019) in the Nkout west prospect. Metamorphism here can be divided into two events. (1) The upper amphibolite to granulite facies stage dominated by garnet formed at temperatures >500 °C. (2) The non-garnet amphibolites reflect lower temperature (200-300°C; Fig. 8b).

Globally, the chemical compositions of metamorphosed BIFs are commonly used to decipher the effects of metamorphism. LILEs such as Ba, K, Rb, Th, and U are mobile during diagenetic and metamorphic processes, thus, are good indicators to detect the effects of metamorphism in the BIF (Ndime *et al.,* 2019). The LILE in the samples from the Njweng prospect are generally very low. This therefore supports their mobility during the process of diagenesis and metamorphism. This is different from the Nkout west BIF that shows a stable behavior in their LILE suggesting that the metamorphosed BIF kept their original chemical compositions during post-depositional processes (Ndime *et al.,* 2019).

5.2. The influence of detrital aluminosilicates on the trace element budget of the BIFs

Precambrian BIFs may serve as proxies that provide information on the chemical composition and the physio-chemical conditions in ambient seawater (Viehmann *et al.,* 2015a,b) at the time of their deposition. The close similarity between the REY distribution in modern seawater and Precambrian marine chemical sediments and, hence, the respective ambient seawater (except for redox sensitive Ce and Eu) provides a robust tool to verify a marine origin of a sequence of chemical sediments (e.g. Bau and Dulski, 1996). Previous studies concluded that BIFs with REY_{SN} patterns sub-parallel to those of modern seawater directly reflect the REEY composition of ancient ambient seawater and can, therefore, be used as prime archives for Precambrian seawater (e.g. Bau and Dulski, 1996; Viehmann *et al.,* 2015a,b). However, only pure chemical sediments are reliable archives of Precambrian seawater and syn- and post depositional processes such as

diagenesis, metamorphic fluid rock alteration and detrital aluminosilicate contributions may alter the pristine seawater signature (e.g. Bau, 1993). The BIFs studied here display typical modern and Archean seawater characteristics in their REY_{SN} patterns, i.e. (i) depletion of $LREY_{SN}$ relative to $HREY_{SN}$, (ii) positive Eu_{SN} and Gd_{SN} anomalies, (iii) super-chondritic Y/Ho ratios (i.e. positive Y_{SN} anomalies) and (iv) lack of Ce_{SN} anomalies (Table 1, Fig. 11). The BIFs also show positive La_{SN} anomalies (Fig.9b). According to Bau and Dulski, (1996) significant La in the BIFs mask the Ce anomaly thus the samples only show a slightly negative Ce anomaly (Fig. 9a). The negative Ce anomaly indicated by the BIFs shows their deposition in an oxidizing environment (Bau and Dulski, 1996). Positive Eu_{SN} anomaly indicates that ambient seawater carried REY that had entered the ocean by moderate-high-temperature hydrothermal fluids (200-300°C, Fig. 8b). These ocean waters are considered as the source of the iron as well as of SiO_2 in the BIFs (Bau *et al.,* 1993). The strong positive Eu anomalies in the BlFs may only result from an input of Eu-enriched hydrothermal fluids into the water column (Alibert *et al.,* 1993).

5.3. Source of chemical components in the BIFs

The source of iron and silica, main components of BIFs, was firstly suggested by Cloud (1973) as derived from seawater. More recently, Klein (2005) proposed a deep ocean derived source for Fe and Si. However, not all BIFs are made up of pure chemical sediments, but some are commonly contaminated by clastic components (Bau and Dulski, 1996; Basta *et al.,* 2011). Thus the composition of Archean chemical sediments reflects input of solutes from both crustal weathering and hydrothermal emissions. Detrital inputs can also occur in shallow water facies iron formation and such clastic particles tend to obscure the seawater signal. The Al_2O_3, Na_2O, K_2O and TiO_2 contents are mainly hosted in silicates and are usually used as contamination input tracers. Such impurities in terrigenous sediments are carried by rivers or winds from weathered pre-existing rock, or deposited by volcanic activities or pelagic sediments (Lascelles, 2007). A strong positive correlation between Al_2O_3 and TiO_2 has been reported for BIF worldwide (Basta *et al.,* 2011; Yang *et al.,* 2015) and is attributed to clastic input. Detrital component in BIF can also be identified through elevated concentrations of HFSE (e.g. Zr, Hf, Ta, and Th), "REE (Bau, 1993) as well as co-variation between HFSE and REE ratios (La/La*, Y/Ho, Pr/Yb, Ce/Ce* (Bau, 1993). Pure chemical sediments are enriched in Mn and Fe but addition of detrital or volcanic material causes their dilution and enrichment of Ti, Al and Zr (Bonatti, 1979). BIFs from this study reveal high contents of SiO_2 and Fe_2O_3 with concentrations that vary from 42.12 to 57.82 wt% SiO_2 and from 38.39 to 54.55 wt% Fe_2O_3. High contents are similar to pure chemical sediment. The low Al_2O_3, TiO_2, Na_2O, K_2O and low concentration of HFSE (Zr, Hf, Ta, Th) coupled with low Nd contents in the BIFs further attest to their detritus-free nature (Figs. 12; Klein, 2005). This is different from BIF reported from the Dales Gorge, Witwatersrand; Elom, Bikoula, Kouambo and Nkout west prospects which records input of detrital material (Pecoits *et al.,* 2009; Viehmann *et al.,* 2015; Ganno *et al.,* 2015, 2017; Teutsong *et al.,* 2017; Ndime *et al.,* 2019).

Furthermore, the BIF investigated in this study shows Fe/Ti ratios that range from 26.85 to 38.15, Fe/Al ratios between 1345.5 and 1907.5 and Si/Al ratios that vary from 1351.5 to 984. This is similar to sediments with predominantly hydrothermal components (Barrett, 1981). On the Si vs Al binary diagram of Choi and Hariya 1992, the BIF samples show hydrothermal signatures (Fig. 8a). Pure hydrothermal deposit contains little Al and high Al/Ti ratio (Marchig *et al.,* 1982). This

is confirmed on the Al-Fe-Mn ternary diagram in which the BIFs plot in the hydrothermal field (Fig. 13) indicating that Si and Fe were likely derived from hydrothermal sources. On the two component diagrams of Alexander *et al.* (2008) the BIF from Njweng plot in the <0.1 high temperature hydrothermal fluid field (Fig. 14a, b). According to the Sm/Yb-Eu/Sm and Y/Ho-Eu/Sm diagrams extremely small amounts of submarine high-T hydrothermal fluids (<0.1%) were enough to cause positive Eu anomalies in the Njweng BIF. Therefore, as observed in BIFs from Dales Gorge; Agus Claras, Elom, Witwatersand, Krivoy Rog, Bikoula, Mbalam and Nkout west (Spier *et al.,* 2007; Ilouga *et al.,* 2013; Viehmann *et al.,* 2015a,b; Ganno *et al.,* 2015, 2017; Teutsong *et al.,* 2017; Chombong *et al.,* 2017; Ndime *et al.,* 2019), it can be deduced that relatively small inputs of high-T hydrothermal fluids may have been sufficient to account for REE-Y distribution in the BIF. All the samples in this study show a positive values for Eu/Eu* (2.65-2.71), which provide an indication of the relative influence of low-temperature hydrothermal fluids and thus distal BIFs deposition relative to fluid vents (Ganno *et al.,* 2017).

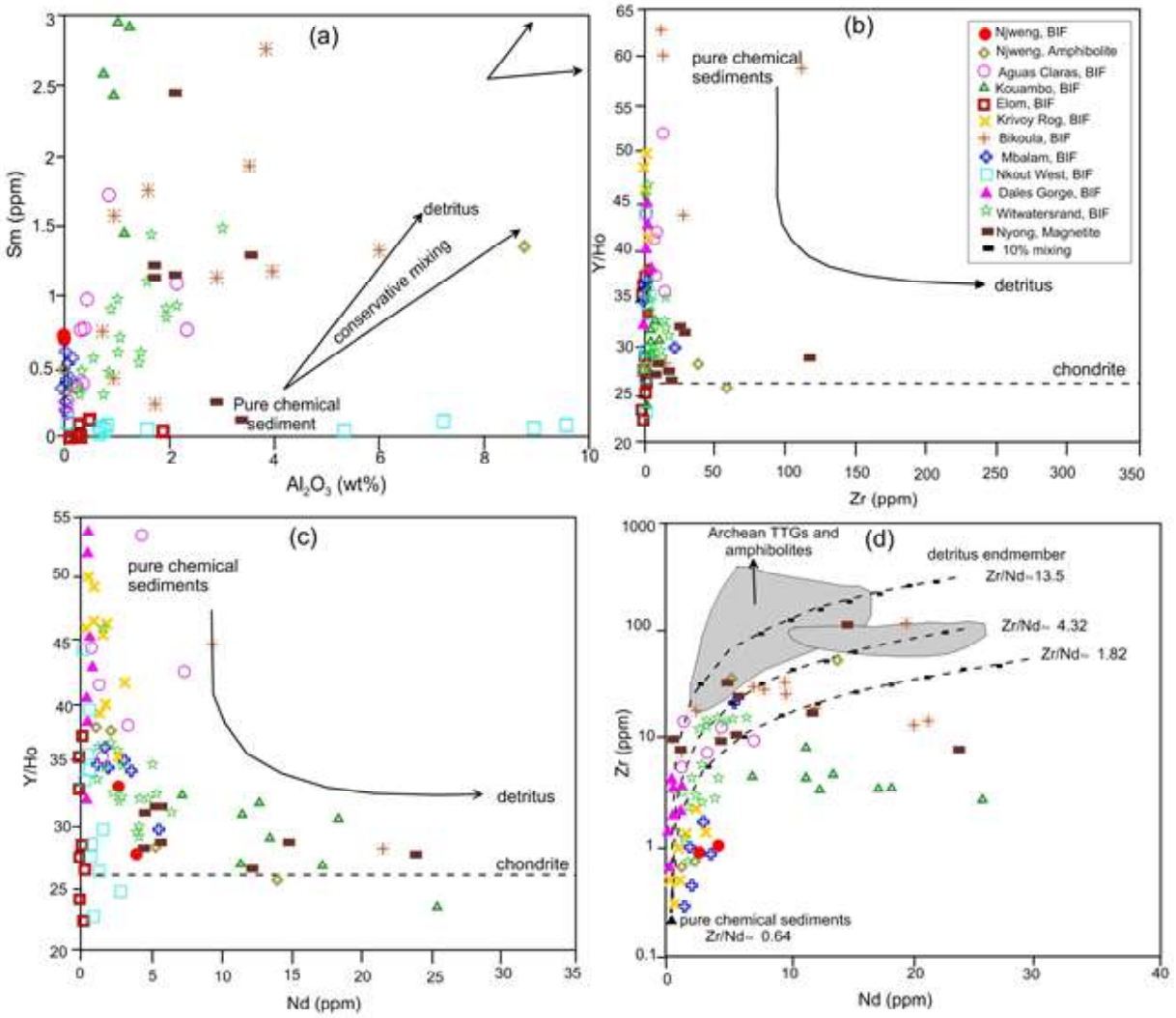

Fig. 12: (a) Graph of Sm vs Al concentrations of BIF from Njweng. b) Graphs of Y/Ho ratios vs Zr concentration, c) Y/Ho ratio vs. Nd concentration. Pure chemical sediments, i.e. the endmember representing seawater, display strongly super-chondritic Y/Ho ratios and low Nd concentrations. With increasing Nd concentration, the Y/Ho ratio in chemical sediments decreases and approaches the Y/

Ho ratios and high Nd concentrations of the schists, revealing significant alteration of the REY budget by detrital aluminosilicates d) Zr vs. Nd of BIFs from the Njweng prospect in comparison to chemical sediments from world class BIFs and BIF deposits in Cameroon. The pure chemical sediment endmember displays the lowest Zr and Nd concentrations and a Zr/Nd ratio of <"0.64. Zr/Nd ratios of possible detritus range from 13.5 to 1.82 and indicate variable supply from the continental hinterland. Conservative mixing lines between endmembers suggest different amounts of aluminosilicate contribution to the BIF during deposition. Additional data are taken from (Spier *et al.,* 2007; Ilouga *et al.,* 2013; Viehmann *et al.,* 2015a,b; Ganno *et al.,* 2015a; 2017; Teutsong *et al.,* 2017; Chombong *et al.,* 2017; Ndime *et al.,* 2019). It is worth noting that high contents of Zr and Nd is significant of detrital input.

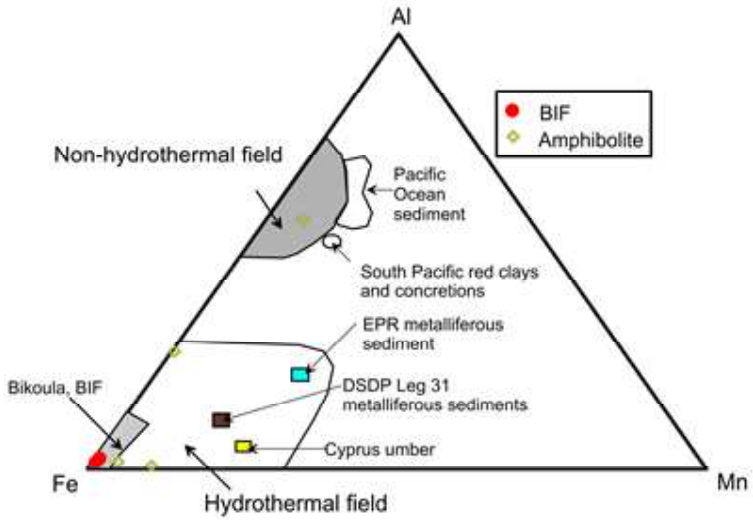

Fig. 13: Ternary Fe-Mn-Al plot showing hydrothermal and non-hydrothermal fields for modern marine ferromanganese deposits (Bostrom, 1973). The Njweng BIF plots within the hydrothermal field. Fields for metalliferous sediments from the East Pacific Rise (EPR) (Bostrom, 1973), Deep Sea Drilling Project (DSDP) Leg 31 (Bonatti *et al.,* 1979), Cyprus umbers (Robertson and Hudson, 1973) and other oceanic sediments are also included. The Njweng BIF is similar to BIF from the Bikoula area (Teutsong *et al.,* 2017)

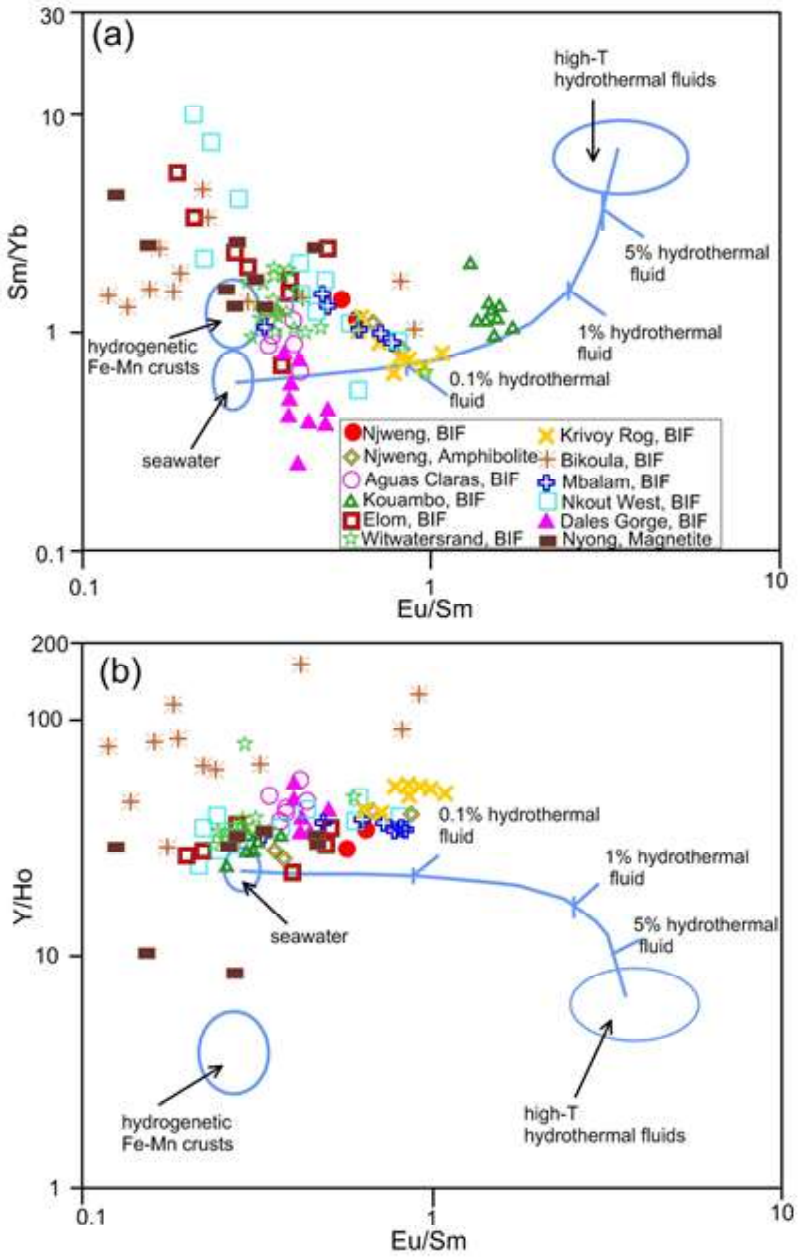

Fig. 14: Composition of the Njweng BIF (triangles) plotted in an elemental ratio diagram with two-component conservative mixing lines for Eu/Sm, Sm/Yb, and Y/Ho (after Alexander *et al.,* 2008). The high-T (N350 °C) hydrothermal fluids follow Bau and Dulski, (1999) and the Pacific seawater follows Alibo and Nozaki, (1999). (a) Plot of Sm/Yb vs. Eu/Sm showing a d" 0.1% high-T hydrothermal fluid contribution. (b) Plot of Y/Ho vs. Eu/Sm showing a d" 0.1% high-T hydrothermal fluid contribution. Additional data are taken from (Spier *et al.,* 2007; Ilouga *et al.,* 2013; Viehmann *et al.,* 2015a,b; Ganno *et al.,* 2015a; 2017; Teutsong *et al.,* 2017; Chombong *et al.,* 2017; Ndime *et al.,* 2019).

5.4. Ore potential of the Njweng BIFs and associated country rocks

The Njweng prospect forms part of the Precambrain iron ore belt of Cameroon with the three main iron ore deposits namely Mbalam, Nkout and the Mamelles (Suh *et al.,* 2008; Ganno *et al.,* 2015). Iron ore deposits within Precambrian BIFs are the most profitable sources of iron making them very attractive exploration targets (Clout, 2006; Duuring *et al.,* 2012). According to Clout, (2006), iron ore can be classified into three groups; (1) Primary unenriched Fe (25-45 wt %), (2) Martite-goethite ore with Fe of 60-63 wt% formed by supergene processes. (3) High grade hematite ore (60 to 68 wt %) formed by hypogene process and subsequently supergene enrichment. According to Klein (2005), the average bulk chemistry of low-grade BIFs from the Archean and Paleoproterozoic are always found to be similar, with Fe_2O_3 ranging from about 20 to 40 wt%. The average concentration of Fe_2O_3 in the BIFs is 46.47 wt% and 30.13 wt% in the amphibolite (Table 1) coupled with relatively high contents of gangue (average of 50 wt %, SiO_2 + Al_2O_3). Deleterious elements such as Al_2O_3, P_2O_5, and TiO_2, are generally low (Table 1). Phosphorous and sulfur represent deleterious elements in the steel making process and are specific targets during iron ore beneficiation (Guider, 1981). The acceptable contents of phosphorous and sulfur in commercial ores should be lower than 0.07% P and 0.1% S, respectively (Guider, 1981). The Njweng BIF shows S contents that are generally below 0.02 wt% which is well below the acceptable average. The phosphorus contents are slightly high (average 0.22%), but within the acceptable levels for commercial ores. Although this can be regarded to as suitable for exploration, the beneficiation process may be problematic (Anderson *et al.,* 2014). Thus the Njweng BIF samples in this study is a magnetite-dominated low grade iron ore, similar to other BIF-hosted iron deposits in Cameroon (e.g. Kouambo iron ore deposit (Ganno *et al.,* 2017), Nkout iron deposit (Suh *et al.,* 2009); Zambi iron deposit (Ganno *et al.,* 2015) and worldwide (e.g. Wittenoom and Mt. Whaleback, Australia (Webb *et al.,* 2006).

Major BIF deposits around the world have recorded gold contents as high as 5 ppm and reserves up to 44.6 Mt (Pereira *et al.,* 2007; Morales *et al.,* 2016; Vitorino *et al.,* 2020). In the Njweng prospect the BIFs and amphibolites show gold contents that reach a maximum of 1.1 and 1.7 ppb, respectively. Gold indices identified in the BIFs and associated rocks are lower than that of world class deposits. Although their contents are low they may serve as potential source of primary gold in the Njweng area and confirm that alluvial gold widely won in the area is derived from the weathering of these rocks.

6. CONCLUSIONS

The following conclusions can be drawn from this studyThe Njweng prospect BIFs occur in association with amphibolites. The BIFs vary from oxide to silicate facies and are composed predominantly of recrystallized quartz associated with magnetite and hematite which are the major ore minerals. The magnetite shows a vuggy texture indicative of leaching of gangue minerals by hypogene fluids

1. The amphibolites bear testament to high grade metamorphic overprint in the area with the development of a granulite facies mineral assemblage

2. The Njweng BIF is predominantly composed of Fe_2O_3 and SiO_2 and their geochemical features indicate pure chemical sediments with no detritus input. Low LILE contents indicate their mobility during the process of diagenesis and metamorphism.

3. The BIF samples display seawater-like "REE-Y features such as Y/Ho ratio ($<$ 43), La/

La^*_{SN} ratio (> 1). This corroborates a detritus-free BIF and an exclusively seawater precipitation of the Njweng BIF.

4. The positive Eu anomaly indicates that metals (Fe and Si) in the Njweng BIF were derived from a high temperature hydrothermal fluid. Negative Ce anomaly implies the anoxic nature of the seawater from which this BIF precipitated.

5. Gold indices identified in the BIFs and associated rocks points to these lithologies as primary gold sources for the alluvial gold workings in the area.

Acknowledgements

AV, DCII and CES acknowledge support from the Cameroon Government through the Research Modernization Allowance scheme of the Ministry of Higher Education that enabled them to fund the M.Sc. dissertation of NCB whose data form part of this contribution. The authors acknowledge the incisive review provided by an anonymous reviewer and the editorial support of Prof. Vincent P.K. Titanji.

REFERENCES

Alexander, B., Bau, M., Andersson, P. and Dulski, P. (2008). Continentally-derived solutes in shallow Archean seawater: rare earth element and Nd isotope evidence in iron formation from the 2.9 Ga Pongola super group. Geochimica et Cosmochimica Acta 72, 378-394.

Alibert, C. and McCulloch, M. T. (1993). Rare earth element and neodymium isotopic compositions of the banded iron formations and associated shales from Hamersley, western Austalia. Geochemica et Cosmochimica Acta 57, 187-204.

Anderson, K. F. E., Wall, F., Rollinson, G. K. and Moon, C. J. (2014). Quantitative mineralogical and chemical assessment of the Nkout iron ore deposit, southern Cameroon. Ore Geology Reviews 62, 25-39.

Angerer, T. and Hagemann, S. G. (2010). BIF hosted high-grade Iron ore deposits in the Archaean Koolyanobbing Greenstone Belt, Western Australia: Structural control on synorogenic and weathering related magnetite, hematite and goethite-rich iron ore. Economic Geology 105, 817-945.

Barrett, T. J. (1981). Chemistry and mineralogy of Jurassic bedded chert overlying ophiolites in the North Appenines, Italy. Chemical Geology 34, 289-317.

Basta, F. F., Maurice, A. E., Fontbote, L. and Favarger, P. (2011). Petrology and geochemistry of the banded iron formation (BIF) of Wadi Karim and Um Anab, Eastern Desert, Egypt: implications for the origin of Neoproterozoic BIF. Precambrian Research 187 277-292.

Bau, M. (1993). Effects of syn- and post-depositional processes on the rare-earth element distribution in Precambrian Iron-formations. European Journal of Mineralogy 5, 257-267.

Bau, M. and Dulski, P. (1996). Distribution of yttrium and rare-earth elements in the Penge and Kuruman iron-formations, Transvaal Supergroup, South Africa. Precambrian Research 79, 37-55.

Biczok, J., Hollings, P., Klipfel, P., Heaman, L., Maas, R., Hamilton, M., Kamo, S. and Friedman, R. (2012). Geochronology of the North Caribou greenstone belt, Superior Province Canada: Implications for tectonic history and gold mineralization at the Musselwhite mine. Precambrian Research 192-195, 209-230.

Bonatti, E., Kolla, V., Moore, W. S. and Stern, C. (1979): Metallogenesis in marginal basins: Fe-rich

basal deposits from the Philippine Sea. Marine Geology, 32, 21-37.

Bonda, B. M. M., Vishiti, A., Mbai S. J., Bayiga E. C., Ngon Ngon, G. F. and Etamé, J. (2022). Microchemical Fingerprint of Magnetite Bearing Iron Ore Deposit from the Sanaga Prospect, Southern Cameroon: Assessment of Iron Ore-forming Conditions. Journal of Geosciences and Geomatics 10, 65-73.

Carlut, J., Isambert, A., Bouquerel, H., Pecoits, E., Philippot, P., Vennin, E., Ader, M., Thomazo, C., Buoncristiani, J-F., Baton, F., Muller, E. and Deldicque, D. (2015). Low temperature magnetic properties of the Late Archean Boolgeeda iron formation (Hamersley Group, Western Australia): environmental implications. Earth Science https://doi.org/10.3389/feart.2015.00018

Choi, J. H. and Hariya, Y. (1992). Geochemistry and depositional environment of Mn Oxide deposits in the Tokoro Belt, Northeastern Hokkaido. Economic Geology 87, 1265-1274.

Chombong, N. N., Suh, C. E., Lehmann, B., Vishiti, A., Ilouga, C. D., Shemang, E. M., Tantoh B. S. and Kedia, A. C. (2017). Host rock geochemistry, texture and chemical composition of magnetite in iron ore in the Neoarchaean Nyong unit in southern Cameroon, Applied Earth Science, DOI: 10.1080/03717453.2017.1345507.

Chombong, N. N. and Suh, C. E. (2013). 2883 Ma commencement of BIF deposition at the northern edge of Congo Craton, southern Cameroon: new zircon SHRIMP data constraint from metavolcanics. Episodes 36, 47-57.

Chombong, N. N., Suh, E.C. and Ilouga, C. D. (2013). New detrital zircon U-Pb ages from BIF-related metasediments in the Ntem Complex (Congo Craton) of southern Cameroon, West Africa. Natural Science 5, 835-847.

Cloud, P. (1973). Paleoecological significance of the banded iron formation. Economic Geology 68, 1135-1143.

Clout, J. M. F. (2006). Iron formation-hosted iron ores in the Hamersley province of Western Australia. Applied Earth Science (Transactions of the Institutions of Mining and Metallurgy: Section B) 115, 115-125.

Dongmo, F. W., Chapman, R. J., Bolarinwa, A. T., Yongue, R. F., Banks, D. A. and Olajide-Kayode, J .O. (2019). Microchemical characterization of placer gold grains from the Meyos Essabikoula area, Ntem complex, southern Cameroon. Journal of African Earth Sciences 151, 181-201.

Duuring, P. and Hagemann, S. G. (2013). Leaching of silica bands and concentration of magnetite in Archaean BIF by hypogene fluids: Beebyn Fe ore deposit, Yilgarn Craton, Western Australia. Mineralum Deposita 48, 341-370.

Duuring, P., Hagemann, S. G., Novikova, Y., Cudahy, T. and Laukamp, C. (2012). Targeting iron ore in banded iron formations using ASTER data: weld range Greenstone Belt, Yilgarn Craton, Western Australia. Economic Geology 107, 585-597.

Fuanya, C., Bolarinwa, A.T., Kankeu, B., Yongue, R.F., Ngatcha, R.B. and Tangko, T.E. (2019). Morphological and chemical assessment of alluvial gold grains from Ako'ozam and Njabilobe, southwestern Cameroon. Journal of African Earth Sciences 154, 111-119.

Ganno, S., Njiosseu, T. E. L., Kouankap, N. G. D., Djoukouo, S. A., Moudioh, C., Ngnotué, T. and Nzenti, J. P. (2017). A mixed seawater and hydrothermal origin of superior-type banded iron

formation (BIF)- hosted Kouambo iron deposit, Palaeoproterozoic Nyong series, Southwestern Cameroon: Constraints from petrography and geochemistry. Ore Geology Reviews 80, 860-875.

Ganno, S., Ngnotue, T., Nono, K. G-D., Nzenti, J. P. and Notsa, F. M. (2015). Petrology and geochemistry of the banded iron-formations from Ntem complex greenstones belt, Elom area, Southern Cameroon: Implications for the origin and depositional environment. Chemie der Erde 75, 375-387.

Guider, J. W. (1981). Iron ore beneûciation key to modern steel making. Min. Eng., 33, 410-413.
Ilouga, D.C. I., Suh, C. E. and Tanwi, G. R. (2013). Textures and rare earth elements composition of banded iron formations (BIF) at Njweng Prospect, Mbalam iron ore district, southern Cameroon. International Journal of Geosciences, 4, DOI:10.4236/ijg.2013.41014

Kimberley, M. M. (1989). Exhalative origins of iron formations. Ore Geology Reviews 5, 13-145.
Klein, C. (2005). Some Precambrian banded iron formations (BIFs) from around the world: Their age, geologic setting, mineralogy, metamorphism, geochemistry and origin. American Mineralogist 90, 1473-1499.

Lascelles, D. F. (2007). Black smokers and the Archean environment: uniformitarian model for the genesis of iron-formations. Ore Geology Reviews 32, 381-411.

Li, X-H., Chen, Y., Li, J., Yang, C., Ling, X-X., Tchouankoue, J. P. (2016). New isotopic constraints on age and origin of Mesoarchaean charnockite, trondhjemite and amphibolite in the Ntem Complex of NW Congo Craton, Southern Cameroon, Precambrian Research, http://dx.doi.org/10.1016/j. precamres.2016.01.027

Marchig, V., Gundlach, H., Möller, P., Schley, F. (1982). Some geochemical indicators for discrimination between diagenetic and hydrothermal metalliferous sediments. Marine Geology 50, 241-256.

McLennan, S. B. (1989). Rare earth elements in sedimentary rocks. Influence of provenance and sedimentary processes In: B.R Lipin and G.A. McKay (Editors), geochemistry and mineralogy of the rare earth elements. Mineralogical Society of America, Washington, 169-200

Milesi, J. P., Toteu, S. F., Deschamps, Y., Feybesse, J. L., Lerouge, C., Cocherie, A., Penaye, J., Tchameni, R., Moloto-A-Kenguemba, G., Kampunzu, H. A. B., Nicol, N., Duguey, E., Leistel, J. M., Saint-Martin, M., Ralay, F., Heinry, C., Bouchot, V., Doumnang Mbaigane, J. C., Kanda Kula, V. Chene, F., Monthel, J., Boutin, P. and Cailteux, J. (2006). "An Overview of the Geology and Major Ore Deposits of Central Africa: Explanatory Note for the 1:4,000,000 Map 'Geology and major ore deposits of Central Africa'". Journal of African Earth Sciences, 4, 571-595.

Morales, M. J., Silva, R. C. F., Lobato, L. M., Gomes, S. D. Gomes, Caio, C. C. O. and Banks D. A. (2016). Metal source and fluid–rock interaction in the Archean BIF-hosted Lamego gold mineralization: Microthermometric and LA-ICP-MS analyses of fluid inclusions in quartz veins, Rio das Velhas greenstone belt, Brazil. Ore Geology Reviews 72, 510-531.

Ndema, M. J. L. and Aroke, E. A. (2020). Petrology and Geochemical Constraints on the Origin of Banded Iron Formation-Hosted Iron Mineralization from the Paleoproterozoic Nyong Serie (Congo Craton, South Cameroon), Pout Njouma Area (Edea North): Evidence for Iron Ore Deposits. International Journal of Research and Innovation in Applied Science, 5, 19 p.

Ndime E. N., Ganno, S., Soh, T. L. and Nzenti, J. P. (2018). Petrography, lithostratigraphy and major element geochemistry of Mesoarchean metamorphosed banded iron formation-hosted Nkout iron ore deposit, north western Congo Craton, Central West Africa. Journal of Earth Sciences 148, 80-98.

Ndime, E. N., Ganno, S. and Nzenti, J. P. (2019). Geochemistry and Pb-Pb geochronology of the Neoarchean Nkout West metamorphosed banded iron formation, Southern Cameroon. International Journal of Earth Sciences 108, 1551-1570.

Nono, G. D. K., Bongsiysi, E. F., Tamfuh, P. A., Abolo, A. J., NKehding, B. F., Kibong, N. F. and Suh, E. C. (2021). Gold deposit type and implication for exploration in the Abiete-Toko Gold District, South Cameroon: constraint from morphology and microchemistryof alluvial gold grains. Heliyon *7(4),* e06758 https://doi.org/10.1016/j.heliyon.2021.e06758

Omang, B. O., Suh, C. E., Lehmann, B., Vishiti, A., Chombong, N. N., Fon, A. N., Egbe, J. A. and Shemang, E.M. (2015). Microchemical signature of alluvial gold from two contrasting terrains in Cameroon. Journal of African Earth Sciences 112, 1-4.

Pecoits, E., Gingras, M. K., Barley, M. E., Kappler, A., Posth, N. R. and Konhauser, K. O. (2009). Petrography and geochemistry of the dales gorge banded iron formation: paragenetic sequence, source and implications for palaeo-ocean chemistry. Precambrian Research 172, 163-187.

Pereira, S. L. M., Lobato, L. M., Ferreira, J. E. and Jardim, E. C. (2007). Nature and origin of the BIF-hosted São Bento gold deposit, Quadrilátero Ferrífero, Brazil, with special emphasis on structural controls. Ore Geology Reviews 32, 571-595.

Pouclet, A., Tchameni, R., Mezger, K., Vidal, M., Nsifa, E.N., Shang, C.K. and Penaye, J. (2007). Archaean crustal accretion at the northern border of the Congo craton (South Cameroon). The charnockite-TTG link. Bulletin de la Société Géologique de France 178, 331-342.

Shang, C. K., Satir, M., Nsifa, E. N., Liegeois, J. P., Siebel, W. and Taubald, H. (2007). Archaean high K granitoids produced by remelting of the earlier Tonalite-Trondhjemite-Granodiorite (TTG) in the Sangmelima region of the Ntem complex of the Congo craton, southern Cameroon. International Journal of Earth Science 96, 817-842.

Shang, C.K., Satir, M., Siebel, W., Nsifa, E.N., Taubald, H., Liegeois, J.P. and Tchoua, F.M. (2004). Major and trace element geochemistry, Rb–Sr and Sm–Nd systematics of TTG magmatism in the Congo craton: case of the Sangmelima region, Ntem complex, southern Cameroon. Journal of African earth Sciences 40, 61-79.

Soh, T. L., Nzepang, T. M., Chongtao, W., Ganno, S., Ngnotued, T., Kouankap, N. G. D., Shaamu, J. S., Zhang, J. and Nzenti, J. P., (2018). Geology and geochemical constrains on the origin and depositional setting of the Kpwa-Atog Boga banded iron formations (BIFs), northwestern Congo Craton, southern Cameroon. Ores Geology Reviews 95, 620-638.

Spier, C. A., Oliveira, S.M.B., Rosière, C. A. and Ardisson, J. D. (2007). Mineralogy and trace element geochemistry of the high-grade iron ores of the Águas Claras Mine and Comparison with the Capão Xavier and Tamanduá iron ore deposits, Quadrilátero Ferrifero, Brazil. Mineralum Deposita, doi 10.1007/s00126-007-0157-z

Spier, C. A., Oliveira, S. M. B., Sial, A. N. and Rois, F. J. (2008). Geochemistry and genesis of the banded iron formation of the Caue Formation,

Quadrilatero Ferrifero, Minas Gerais, Brazil. Precambrian Research 152, 170-206.

Suh, C. E., Cabral, A. R., Shemang, E. M., Mbinkar, L. and Mboudou, G.G. M. (2008). Two contrasting iron deposits in the Precambrian mineral belt of Cameroon, West Africa. Exploration and Mining Geology 17, 197-207.

Suh, C. E., Cabral, A. and Ndime, E. N. (2009). Geology and ore fabrics of the Nkout high grade haematite deposit, southern Cameroon. Smart Science Exploration Mineral 1, 558-560.

Sun, S.-S. and McDonough, W.F. (1989). Chemical and isotopic systematics of oceanic basalts: implications for mantle composition and processes. Geochemical Society of London Special Publication 42, 313-345.

Takam, T., Arima, M., Kokonyangi, J., Dunkley, D. J. and Nsifa, E. N. (2009). Paleoarchaean charnockites in the Ntem complex, Congo craton, Cameroon: insights from SHRIMP zircon U–Pb ages. Journal of Mineralogical and Petrological Science 104, 1-11.

Tchameni, R., Mezger, K., Nsifa, N. E. and Pouclet, A. (2001). Crustal origin of Early Proterozoic syenites in the Congo Craton (Ntem Complex), south Cameroon. Lithos 57, 23-42.

Teutsong, T., Bontognali, T. R. R., Ndjigui, P-D., Vrijmoed, J. C., Teagle, D., Cooper, M. and Vance, D. (2017). Petrography and geochemistry of the Mesoarchaean Bikoula banded iron formation in the Ntem Complex (Congo Craton), southern Cameroon: Implications for origin. Ore Geology Reviews 80, 267-288.

Van Schmus, W.R., Oliveira, E.P., Da Silva Filho, A.F., Toteu, S.F., Penaye, J. and Guimarães, I.P. (2008). The Central African Fold Belt Proterozoic links between the Borborema Province, NE Brazil, and the Central African Fold Belt. Geological Society, London, Special Publications 294, 69-99.

Viehmann, S., Bau, M., Smith, A. J. B., Beukes, N. J., Dantas, E. L. and Bühn, B. (2015a). The reliability of ~2.9 Ga old Witwatersrand banded iron formations (South Africa) as archives for Mesoarchaean seawater: Evidence from REE and Nd isotope systematic. Journal of African Earth Sciences 111, 322-334.

Viehmann S., Bau M., Hoffmann J. E., Münker C. (2015b). Geochemistry of the Krivoy Rog Banded Iron Formation, Ukraine, and the impact of peak episodes of increased global magmatic activity on the trace element composition of Precambrian seawater. Precambrian Research 270, 165-180.

Vitorino, A. L. A. Figueiredo Silva R. C. and Lobato, L. M. (2020). Shear-zone-related gold mineralization in quartz-carbonate veins from metamafic rocks of the BIF-hosted world-class Cuiabá deposit, Rio das Velhas greenstone belt, Quadrilátero Ferrífero, Brazil: vein classification and structural control, Ore Geology Reviews doi: https://doi.org/10.1016/j.oregeorev.2020.103789

Webb, A. D., Dickens, G. R. and Oliver, N. H. S. (2006). Carbonate alteration of the Upper Mount McRae Shale at Mount Whaleback, Western Australia – implications for iron ore genesis. Applied Earth Science (Transactions of the Institutions of Mining and Metallurgy: Section B), 115, 161-166

Yang, X-Q, Zhang, Z-H, Duan, S-G and Zhao, X-M (2015). Petrological and geochemical features of the Jingtieshan banded iron formation (BIF): a unique type of BIF from the Northern Qilian Orogenic Belt, NW China. Journal of Asian Earth Sciences 113, 1218-1234

www.sundanceresources.com.au